Acta Polytechnica **62**(1):38–49, 2022
https://doi.org/10.14311/AP.2022.62.0038

Published by the Czech Technical University in Prague

ABOUT THE TIME EVOLUTION OF COHERENT ELECTRON STATES IN MONOLAYERS OF BORON ALLOTROPES

Erik Díaz-Bautista

Instituto Politécnico Nacional, Unidad Profesional Interdisciplinaria de Ingeniería Campus Hidalgo, Departamento de Formación Básica Disciplinaria, Ciudad del Conocimiento y la Cultura, Carretera Pachuca-Actopan km 1+500, San Agustín Tlaxiaca, 42162 Hidalgo, México

correspondence: ediazba@ipn.mx

Abstract. In this paper, we theoretically analyze the massless Dirac fermion dynamics in two-dimensional monolayers of boron allotropes, 8B and 2BH $-$ *pmmn* borophene, interacting with external electric and magnetic fields. We study the effect of the Dirac cone tilt in these materials, which is known as valley index, through the time evolution of probability density of coherent electron states as well as their phase-space representation obtained via the Wigner function. Our results show that the time evolution of the coherent electron states in these materials is valley dependent, which is reinforced in the presence of external electric fields.

Keywords: Tilted Dirac cones, anisotropic Dirac materials, borophene, coherent states, Wigner function.

1. Introduction

Coherent states (CSs) are minimal uncertainty states [1, 2], so that they are considered the most classical states in quantum mechanics. For this reason, they arise in multiple branches of physics, mainly in quantum optics [2] and information processes [3, 4]. Although the wave function provides interesting features about any state, its experimental realization in several quantum systems [3] requires a different approach. In this sense, the Wigner function (WF) constitutes one of the most important theoretical tools for describing quantum systems in the phase-space representation. The WF for a bidimensional system is a quasi-probability distribution defined as [5–7]

$$W(\mathbf{r},\mathbf{p}) = \frac{1}{(2\pi)^2}\int_{-\infty}^{\infty} \mathrm{e}^{i\,\mathbf{p}\cdot\mathbf{q}}\,\Psi\left(\mathbf{r}-\frac{\mathbf{q}}{2}\right)\Psi^{\dagger}\left(\mathbf{r}+\frac{\mathbf{q}}{2}\right)d\mathbf{q}, \tag{1}$$

where $\Psi(\mathbf{r})$ is the wave function, $\mathbf{r} = (x, y)$ and $\mathbf{p} = (p_x, p_y)$ are two-dimensional vectors representing the classical position and momentum values in phase space, respectively; and $\mathbf{q} = (q_1, q_2)$ is a position vector needed in the integration process. In contrast with the probability density of any quantum state, the WF can take negative values, which indicates the nonclassicality of a state and it is a sign of quantumness [3, 8, 9]. Despite this, it has been implemented in quantum optics [3, 4, 9–13], and recently also applied in condensed matter for studying electron dynamics in two-dimensional materials, particularly in graphene under the presence of electromagnetic fields [3, 14–26] as well as in strained honeycomb lattices with dispersive pseudo-Landau-levels [27].

Following this trend, and since the number of two-dimensional materials has been increasing recently, our aim is to provide an adequate description in phase space of the physics of certain quantum macroscopic phenomena, and their semi-classical representation, that occurs in condensed matter systems in the context of valleytronics [28–30]. In this emerging research area, two-dimensional materials such as $8-pmmn$ borophene [31–35], strained graphene [36], Weyl semimetals [37–40], and the organic compound α-(BEDT-TTF)$_2$I$_3$ [41–44], characterize due to the presence of anisotropy and tilted Dirac cones at their low-energy band structure [31, 32, 40, 43, 45–53]. The anisotropy and tilt can be intrinsic, as occurs in borophene [31–34] and phosphorene [54, 55], or induced by strain-engineering and external electric fields, as observed in graphene [20, 36, 56–72].

In this work, we will focus on two-dimensional monolayers of boron allotropes, 8B and 2BH $-$ *pmmn* borophene [73], which have recently attracted attention due to the boron capacity of flexible bonding [47, 74, 75]. The geometry of two-dimensional boron-based Dirac cone materials is much more complicated than that of the pristine honeycomb structure of graphene and, as a consequence, their electronic and transport properties are valley dependent due to the tilting of Dirac cones. These features motivate the research of unusual effects by the intrinsic Dirac cone tilt under the presence of external electric and magnetic fields. For instance, the study of $8-pmmn$ borophene conductivity in the presence of crossed electric and magnetic fields exhibits a clear valley-dependence in magnetotransport properties and polarization currents [33, 34]. It exists the possibility of the realization of coherent electron states in the laboratory and the development of electron quantum optics [15, 76, 77] due to the recent advances in the experimental reconstruction of the WF of electronic systems in quantum tomography experiments.

Thus, this paper is organized as follows. In Section 2, we describe the Dirac Hamiltonian of monolayers of boron allotropes at low-energy regime in the presence of external electric and magnetic fields, and obtain the corresponding Landau states and energy spectra. In Section 3, we discuss the construction of the matrix ladder operators associated to the physical system and also construct the corresponding coherent electron states as eigenstates of the annihilation operator. We also study the time evolution of the probability density and the corresponding phase-space representation. In Section 4, we present our conclusions.

2. Electron dynamics in monolayers of boron allotropes

$8-pmmn$ borophene [31–34] and other two-dimensional monolayers of boron allotropes, such as 8B and 2BH $-pmmn$ borophene [73], present tilted Dirac cones at their low electronic band structure, so that their electronic properties are described by the continuous Dirac Hamiltonian

$$H = \nu\,(v_t\sigma_0 p_y + v_x\sigma_x p_x + v_y\sigma_y p_y), \tag{2}$$

where the matrices $\sigma_{x,y}$ are the Pauli matrices, while σ_0 is the identity matrix. The quantity ν, known as valley index, allows us to transit from valley K ($\nu = 1$) to valley K' ($\nu = -1$). The terms v_x and v_y are the anisotropic Fermi velocities and v_t is the velocity that quantifies the tilting of the Dirac cone. These velocities depend on the material. For instance, the velocity values $\{v_x, v_y, v_t\}$ in multiples of the Fermi velocity $v_\mathrm{F} = 1$ for three different allotropes of boron are shown in Table 1.

Boron allotrope	v_x	v_y	v_t
$8-pmmn$	0.86	0.69	0.32
8B $-pmmn$	0.534	0.785	-0.345
2BH $-pmmn$	0.77	1.348	-0.386

Table 1. The velocities v_x, v_y and v_t in units of the Fermi velocity $v_\mathrm{F} = 10^6$ m/s, for three boron allotropes in the low-energy single-particle effective model.

2.1. Effective Dirac-Weyl Hamiltonian

Now, let us consider massless Dirac fermions in a two-dimensional boron monolayer under the presence of an in-plane electric field $\mathbf{E} = \mathcal{E}\hat{x}$ and a perpendicular magnetic field $\mathbf{B} = B\hat{z}$. These fields are included in the Hamiltonian in Eq. (2) through the scalar and vector potentials

$$U = -x\,\mathcal{E}, \quad \mathbf{A} = x\,B\hat{y}, \tag{3}$$

to obtain the following eigenvalue equation in natural units ($e = -1$ and $\hbar = 1$) [35, 42, 43]:

$$\begin{aligned} &H'\bar{\Psi}(\mathbf{r}) \\ &= (\nu\,[v_x\sigma_x p_x + (v_t\sigma_0 + v_y\sigma_y)(p_y + xB)] + x\mathcal{E}\sigma_0)\,\bar{\Psi}(\mathbf{r}) \\ &= E\bar{\Psi}(\mathbf{r}). \end{aligned} \tag{4}$$

Taking advantage of the translational invariance along the y-axis, so that $\bar{\Psi}(\mathbf{r}) = \exp(iky)\Psi(x)$, the eigenvalue equation in Eq. (4) becomes:

$$\left[\left(\frac{\overline{E} - x_c\,\overline{\mathcal{E}}}{v'_\mathrm{F}}\right)\sigma_0 + i\partial_x\sigma_x - \frac{\left(x_c\,\omega_\mathrm{B} + 2k_y^c\right)}{2}\sigma_y\right]\Psi(x) = 0, \tag{5}$$

where $\overline{E} = E - \nu\,v_t k_y$, $\overline{\mathcal{E}} = (\mathcal{E} + \nu\,v_t B)\sqrt{v_x/v_y}$, $\omega_\mathrm{B} = 2B$, $x_c = x\sqrt{v_y/v_x}$, $k_y^c = k_y\sqrt{v_y/v_x}$, and $v'_\mathrm{F} = \sqrt{v_x v_y}$ is an effective Fermi velocity. By introducing the parameter β_ν and the dimensionless quantity ξ,

$$\beta_\nu = \frac{\overline{\mathcal{E}}}{v'_\mathrm{F}B} = \frac{v_\mathrm{d}}{v_y} + \nu\frac{v_t}{v_y}, \quad \xi = \sqrt{\frac{\omega_\mathrm{B}}{2}}\left(x_c + \frac{2k_y^c}{\omega_\mathrm{B}}\right), \tag{6}$$

with $v_\mathrm{d} = \mathcal{E}/B$ being the drift velocity, Eq. (5) can be rewritten as

$$\left[\left(\epsilon_0 - \sqrt{\frac{\omega_\mathrm{B}}{2}}\beta_\nu\xi\right)\sigma_0 + i\sqrt{\frac{\omega_\mathrm{B}}{2}}\frac{\mathrm{d}}{\mathrm{d}\xi}\sigma_x - \sqrt{\frac{\omega_\mathrm{B}}{2}}\xi\sigma_y\right]\Psi(\xi) = 0, \tag{7}$$

where $\epsilon_0 = \overline{E}/v'_\mathrm{F} + k_y^c\beta_\nu = (E + k_y v_\mathrm{d})/v'_\mathrm{F}$.

2.1.1. Energy spectrum

In order to find the solutions of the initial problem, we proceed as follows [78, 79]. Multiplying by $-i\sigma_x$ to the left of Eq. (7), we get:

$$\begin{aligned}\left[\sqrt{\frac{\omega_\mathrm{B}}{2}}\frac{\mathrm{d}}{\mathrm{d}\xi}\sigma_0 - i\left(\epsilon_0 - \sqrt{\frac{\omega_\mathrm{B}}{2}}\beta_\nu\xi\right)\sigma_x\sigma_0\right. \\ \left. + i\sqrt{\frac{\omega_\mathrm{B}}{2}}\xi\sigma_x\sigma_y\right]\Psi(\xi) = 0. \end{aligned} \tag{8}$$

Differentiating the above expression with respect to ξ, we obtain the following equation

$$\left[\left(\frac{\mathrm{d}^2}{\mathrm{d}\xi^2} + \left(\sqrt{\frac{2}{\omega_\mathrm{B}}}\epsilon_0 - \beta_\nu\xi\right)^2 - \xi^2\right)\sigma_0 + \mathbb{K}\right]\Psi(\xi) = 0, \tag{9}$$

where $\mathbb{K} = i\,(\sigma_x\beta_\nu + \sigma_x\sigma_y)$ is a complex symmetric matrix. The solutions of Eq. (9) can be expressed as $\Psi(\xi)_\eta = \psi_\eta(\xi)\chi_\eta$, where χ_η fulfills the eigenvalue equation $\mathbb{K}\chi_\eta = \eta\chi_\eta$, and $\psi_\eta(\xi)$ is a scalar function that satisfies the differential equation

$$\left[\frac{\mathrm{d}^2}{\mathrm{d}\xi^2} + \left(\sqrt{\frac{2}{\omega_\mathrm{B}}}\epsilon_0 - \beta_\nu\xi\right)^2 - \xi^2 + \eta\right]\psi_\eta(\xi) = 0. \tag{10}$$

In order to simplify the above equation, the variable ζ is defined as

$$\zeta = \xi(1 - \beta_\nu^2)^{1/4} + \sqrt{\frac{2}{\omega_\mathrm{B}}}\frac{\beta_\nu\,\epsilon_0}{(1 - \beta_\nu^2)^{3/4}}, \tag{11}$$

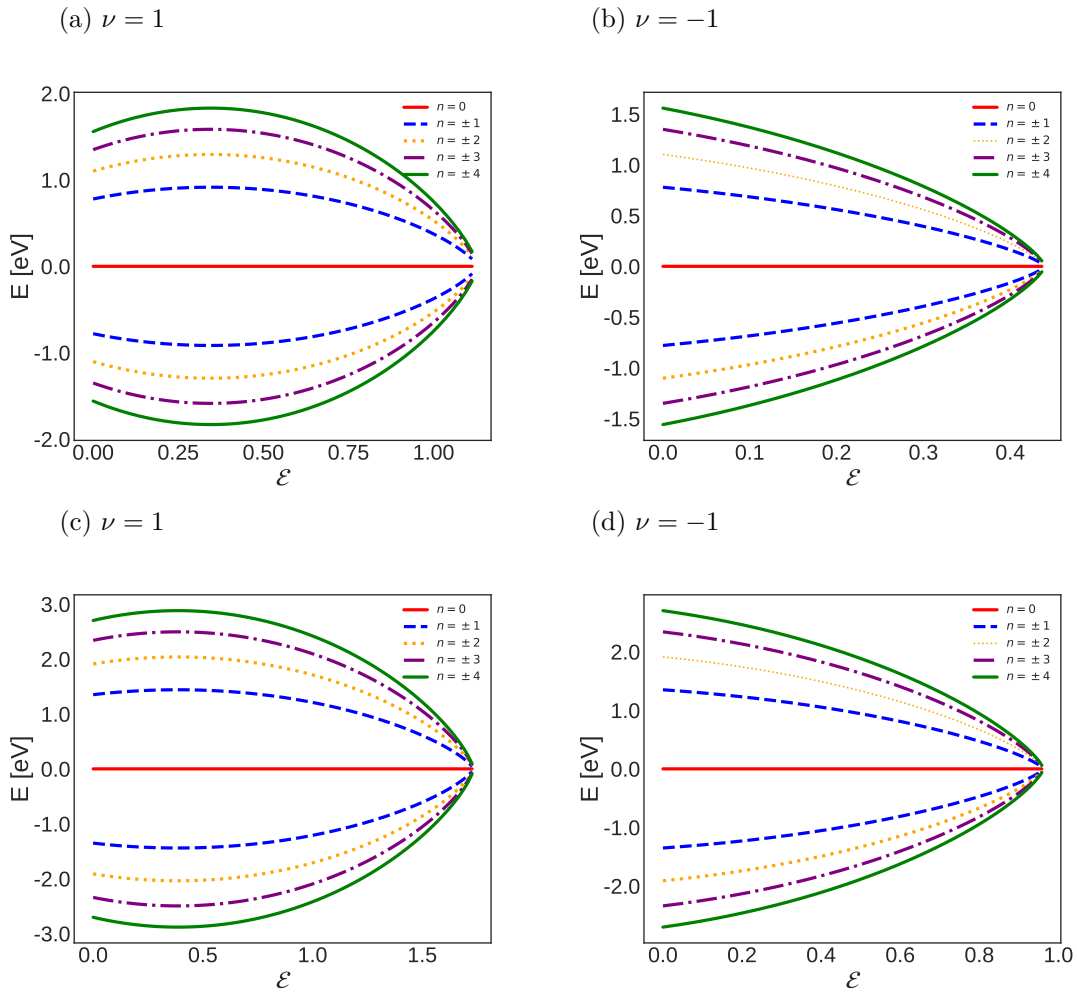

FIGURE 1. Energy spectrum in Eq. (15) with $k_y = 0$ and $B = 1$ as a function of the electric field $\mathcal{E}$ for 8B $-$ *pmmn* borophene (a, b) and 2BH $-$ *pmmn* (c, d) in each Dirac point ($\nu = \pm 1$).

where β_ν must fulfill the condition $|\beta_\nu| < 1$ for keeping real values of ζ. Hence, we obtain the Weber equation

$$\left[\frac{\mathrm{d}^2}{\mathrm{d}\zeta^2} - \zeta^2 + \frac{2\epsilon_0^2}{\omega_{\mathrm{B}}(1-\beta_\nu^2)^{3/2}} + \frac{\eta}{(1-\beta_\nu^2)^{1/2}}\right]\psi_\eta(\zeta) = 0. \tag{12}$$

On the other hand, the eigenvalues η of the matrix $\mathbb{K}$ turn out to be $\sigma(\mathbb{K}) = \{\eta_k = (-1)^k(1-\beta_\nu^2)^{1/2}\}$ with $k = 1, 2$, while the corresponding normalized eigenvectors are given by

$$\chi_{\eta_1} = \frac{1}{\sqrt{2}}\begin{pmatrix} \sqrt{C_+} \\ -i\sqrt{C_-} \end{pmatrix}, \quad \chi_{\eta_2} = \frac{1}{\sqrt{2}}\begin{pmatrix} -\sqrt{C_-} \\ i\sqrt{C_+} \end{pmatrix}, \tag{13}$$

where $C_\pm = 1 \pm \sqrt{1-\beta_\nu^2}$. Substituting the eigenvalues η_k in Eq. (12) and taking $\psi_\eta(\zeta) = \exp\left(-\zeta^2/2\right) f_\eta(\zeta)$, one gets the following ODE:

$$f_\eta''(\zeta) - 2\,\zeta f_\eta'(\zeta) = \left(1 - (-1)^k - \frac{2\epsilon_0^2/\omega_{\mathrm{B}}}{(1-\beta_\nu^2)^{3/2}}\right) f_\eta(\zeta), \tag{14}$$

with $k = 1, 2$. By solving the above ODE, the energy spectrum turns out to be [80] (see Figure 1):

$$E_{n,k_y} = \mathrm{sgn}(n)\sqrt{v_x v_y}(1-\beta_\nu^2)^{3/4}\sqrt{\omega_{\mathrm{B}}|n|} - k_y\, v_{\mathrm{d}}. \tag{15}$$

The Landau energy levels in Eq. (15) depend on valleys K and K' [43] via the amount β_ν in Eq. (6), which indicates whether the orbits are closed ($|\beta_\nu| < 1$) or opened ($|\beta_\nu| \geq 1$) [43, 80, 81]. Also, the critical values of $v_{\mathrm{d}}^c = \mathcal{E}_c$ for which $\beta_\nu = 1$ depend on each tilted anisotropic Dirac material (see again Figure 1). For instance, in Table 2 we summarize the critical values $\mathcal{E}_c$ in valleys K and K' for three monolayers of boron allotropes.

Borophene monolayer	$\mathcal{E}_c$ (K)	$\mathcal{E}_c$ (K')
$8 - pmmn$	0.37	1.01
8B $-$ *pmmn*	1.13	0.44
2BH $-$ *pmmn*	1.734	0.962

TABLE 2. The electric field critical value $\mathcal{E}_c = (v_y - \nu v_t)B$ for three boron allotropes according to the valley index ν. The data for $8 - pmmn$ borophene were obtained from [35].

Finally, the average velocity in the y-direction is given by [82, 83]

$$\langle v_y \rangle = \frac{\partial E_{n,ky}}{\partial k_y} = -v_{\rm d} = \left[\frac{\mathbf{E} \times \mathbf{B}}{B^2} \right]_y , \qquad (16)$$

that means the Dirac fermions move with an average velocity $v_{\rm d}$ in the negative y-direction.

2.1.2. Eigenstates

The eigenstates of the Hamiltonian in Eq. (4) can be written as

$$\Psi_n(x) = \frac{[(1-\delta_{0n})\chi_{\eta_1}\psi_{n-1}(x) + \lambda\chi_{\eta_2}\psi_n(x)]}{\sqrt{2^{(1-\delta_{0n})}}} = \mathbb{M}\Phi_n(x), \qquad (17)$$

where δ_{mn} denotes the Kronecker delta, the band index λ indicates the conduction ($\lambda = 1$) or ($\lambda = -1$) valence band, and

$$\mathbb{M} = \sqrt{\frac{1}{2}} \begin{pmatrix} \sqrt{C_+} & i\sqrt{C_-} \\ -i\sqrt{C_-} & \sqrt{C_+} \end{pmatrix}, \qquad (18a)$$

$$\Phi_n(x) = \frac{1}{\sqrt{2^{(1-\delta_{0n})}}} \begin{pmatrix} (1-\delta_{0n})\psi_{n-1}(x) \\ i\lambda\,\psi_n(x) \end{pmatrix}. \qquad (18b)$$

The components of the pseudo-spinor $\Phi_n(x)$ are given by the wave functions [79]

$$\psi_n(\zeta_n) = \frac{(1-\beta_\nu^2)^{1/8}}{\sqrt{n!}} \left(\frac{\omega_{\rm B} v_y}{2\pi v_x} \right)^{1/4} D_n(\sqrt{2}\,\zeta_n), \qquad (19)$$

where $D_n(\cdot)$ are the parabolic cylinder functions with n a non-negative integer, and the quantity ζ_n is given by Eq. (11) with $\epsilon_0 = (E_{n,k_y} + k_y v_{\rm d})/\sqrt{v_x v_y}$.

3. Coherent electron states

We start to obtain the CSs by first considering the set of ladder operators $\mathbb{A}^\pm$ given in [35] and acting on the Hilbert basis $\Phi_n(x) = \mathbb{M}^{-1}\Psi_n(x)$, namely,

$$\mathbb{A}^+\Phi_n(\zeta_n) = \sqrt{2^{(1-\delta_{0n})}}\sqrt{n+1}\,\Phi_{n+1}(\zeta_{n+1}), \qquad (20a)$$

$$\mathbb{A}^-\Phi_n(\zeta_n) = \sqrt{2^{(1-\delta_{1n})}}\sqrt{n}\,\Phi_{n-1}(\zeta_{n-1}), \qquad (20b)$$

and whose commutation relation reads

$$[\mathbb{A}^-, \mathbb{A}^+]\Phi_n(x) = c(n)\Phi_n(x), \quad c(n) = \begin{cases} 1, & n = 0, \\ 3, & n = 1, \\ 2, & n > 1. \end{cases} \qquad (21)$$

Now, we define the CSs as eigenstates of the annihilation operator $\mathbb{A}^-$:

$$\mathbb{A}^-\Phi_z(x) = z\,\Phi_z(x), \quad z \in \mathbb{C}, \qquad (22)$$

with complex eigenvalue, where

$$\Phi_z(x) = \sum_{n=0}^{\infty} a_n \Phi_n(x). \qquad (23)$$

Using Eq. (20a), the explicit expression for the CSs is given by

$$\Phi_z(x) = \mathcal{N}_\alpha \left[\Phi_0(x) + \sum_{n=1}^{\infty} \frac{\sqrt{2}\alpha^n}{\sqrt{n!}} \Phi_n(x) \right], \qquad (24)$$

where $\mathcal{N}_\alpha^{-2} = 2\exp\left(|\alpha|^2\right) - 1$ and $\alpha = z/\sqrt{2} = |\alpha|\exp(i\varphi)$. Here, the physical meaning of $|\alpha|$ is that it is the oscillation amplitude while the phase angle φ is identical to the angular rotation in the classical motion. It is worth to mention that the procedure described allows to obtain the so-called Barut-Girrardello CSs. However, this is not the only way to build CSs. In [27], the displacement-operator method has been implemented in order to construct such states in other honeycomb lattices.

Finally, defining the matrix operators

$$\mathbb{B}^- \equiv \mathbb{M}\,\mathbb{A}^-\mathbb{M}^{-1}, \quad \mathbb{B}^+ \equiv \mathbb{M}\,\mathbb{A}^+\mathbb{M}^{-1}, \qquad (25)$$

whose actions on the Landau states $\Psi_n(x)$ in Eq. (17) reads as

$$\mathbb{B}^+\Psi_n(\zeta_n) = \sqrt{2^{(1-\delta_{0n})}}\sqrt{n+1}\,\Psi_{n+1}(\zeta_{n+1}), \qquad (26a)$$

$$\mathbb{B}^-\Psi_n(\zeta_n) = \sqrt{2^{(1-\delta_{1n})}}\sqrt{n}\,\Psi_{n-1}(\zeta_{n-1}), \qquad (26b)$$

it is possible to verify that the states $\Psi_\alpha(x) = \mathbb{M}\,\Phi_z(x)$ are eigenfunctions of the annihilation operator $\mathbb{B}^-$ with the same eigenvalue z. Therefore, the states $\bar{\Psi}_\alpha(\mathbf{r}) = \exp(ik_y y)\,\Psi_\alpha(x)$ are the coherent electron states of the system. In addition, the commutation relation in Eq. (21) is also fulfilled writing $\mathbb{B}^\pm$ and Ψ_n instead of $\mathbb{A}^\pm$ and Φ_n, respectively.

3.1. Overcompleteness and resolution to the identity

The CSs satisfy the following relation

$$|\langle\bar{\Psi}_{\alpha'}|\bar{\Psi}_\alpha\rangle| = \left| \frac{2\exp(\alpha'^*\alpha) - 1}{\sqrt{(2\exp(|\alpha|^2) - 1)(2\exp(|\alpha'|^2) - 1)}} \right| \neq \delta(\alpha' - \alpha). \qquad (27)$$

Since the coherent electron states are not orthogonal for $\alpha \neq \alpha'$, we say the set of such states is overcomplete.

Besides, these CSs satisfy the following relation that can be considered as an unusual resolution to the identity:

$$\frac{|\bar{\Psi}_0\rangle\langle\bar{\Psi}_0|}{2} + \int_{\mathbb{C}} \frac{{\rm d}\rho(\alpha)}{\pi} |\bar{\Psi}_\alpha\rangle\langle\bar{\Psi}_\alpha| = \mathbb{I}_+, \qquad (28)$$

where $\mathbb{I}_+$ denotes the identity operator in the Hilbert space for Landau states in the conduction band, and ${\rm d}\rho(\alpha)$ is a positive measure defined as

$${\rm d}\rho(\alpha) = \frac{2\exp\left(|\alpha|^2\right) - 1}{2\exp\left(-|\alpha|^2\right)} |\alpha|\,{\rm d}|\alpha|\,{\rm d}\varphi. \qquad (29)$$

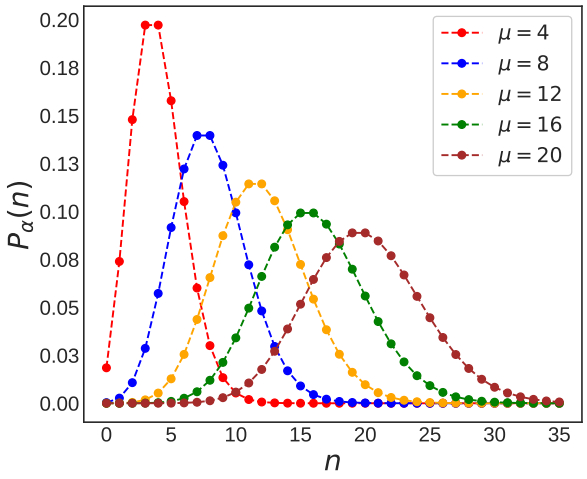

Figure 2. Occupation number distribution $P_\alpha(n)$ in Eq. (30) for the coherent electron states $\bar{\Psi}_\alpha$ for different values of $\mu = |\alpha|^2$.

3.2. Occupation number distribution

The CSs follow a Poisson-like distribution with mean $\mu = |\alpha|^2$, according to the occupation number distribution

$$P_\alpha(n) = |\langle \bar{\Psi}_n | \bar{\Psi}_\alpha \rangle| = \frac{1}{2\exp(\mu) - 1} \begin{cases} 1, & n = 0, \\ \frac{2\mu^n}{n!}, & n > 0, \end{cases} \tag{30}$$

which gives the probability of a CS of being in an Landau state $\bar{\Psi}_n$ (see Figure 2).

3.3. Mean energy value

On the another hand, the expectation value of the energy in the CS basis is given by

$$\langle H \rangle_\alpha = \mathcal{N}_\alpha^2 \Bigg[k_y v_\mathrm{d} \left(1 - 2\exp\left(|\alpha|^2\right)\right) + 2\sqrt{v_x v_y \omega_\mathrm{B}} \times (1 - \beta_\nu^2)^{3/4} \sum_{n=1}^{\infty} \mathrm{sgn}(n) \frac{|\alpha|^{2n}}{n!} \sqrt{|n|} \Bigg]. \tag{31}$$

The mean group velocity of the CSs is obtained as

$$\langle v_y \rangle_\alpha = \frac{\partial \langle H \rangle_\alpha}{\partial k_y} = -v_\mathrm{d}, \tag{32}$$

which agrees with Eq. (16).

3.4. Time evolution of the wave packet

Now, let us consider the time-evolution operator $U(t) = \exp(-iHt)$ applied on the expansion of CSs in terms of Landau states $\bar{\Psi}_n(\mathbf{r})$. Hence, the time-dependent coherent electron states are:

$$\bar{\Psi}_\alpha(\mathbf{r}, t) = \mathcal{N}_\alpha \exp(ik_y y)\, \mathbb{M} \begin{pmatrix} \psi_{\alpha,1}(x,t) \\ i\,\lambda\, \psi_{\alpha,2}(x,t) \end{pmatrix}, \tag{33}$$

where

$$\psi_{\alpha,1}(x,t) = \sum_{n=1}^{\infty} \frac{\alpha^n \mathrm{e}^{-iE_n t}}{\sqrt{n!}} \psi_{n-1}(x), \tag{34a}$$

$$\psi_{\alpha,2}(x,t) = \sum_{n=0}^{\infty} \frac{\alpha^n \mathrm{e}^{-iE_n t}}{\sqrt{n!}} \psi_n(x). \tag{34b}$$

The time-dependent probability density $|\bar{\Psi}_\alpha(\mathbf{r}, t)|^2$ is

$$|\bar{\Psi}_\alpha(\mathbf{r}, t)|^2 = \mathcal{N}_\alpha^2 \Big\{ |\psi_{\alpha,1}(x,t)|^2 + |\psi_{\alpha,2}(x,t)|^2 - 2\lambda\beta_\nu \Re\left[\psi_{\alpha,1}^*(x,t)\psi_{\alpha,2}(x,t)\right] \Big\}, \tag{35}$$

where $\Re(z)$ denotes the real part of a complex number z.

Figure 3 shows the time evolution of the probability distribution of the CSs for 8B and 2BH $-pmmn$ borophene. We can see that in both cases, the density probability in valley K evolves faster than that in valley K'. This means that Dirac fermions take less time to complete a loop around the equilibrium point. The function $|\bar{\Psi}_\alpha(\mathbf{r}, t)|^2$ shows maximum values close to the turning points in the x-axis. Besides, with the values chosen for the parameters $\alpha = 4i$, $k_y = 0$ and $B = 1$, the probability density of the CSs with $\nu = -1$ for 8B $-pmmn$ borophene shows a different behavior in time in comparison to the other cases. This is related to the fact for the electric field considered ($\mathcal{E} = 0.25$), the corresponding energy spectrum is near to collapse, indicating the classical orbits that the charge carriers in valley K' follow are more open compared with those in K for 8B $-pmmn$ borophene, and even for those ones in 2BH $-pmmn$ borophene.

3.5. Obtaining of the time-dependent Wigner function for coherent electron states

To calculate the Wigner matrix (WM) [84] for the coherent states in Eq. (33) in valleys K and K', we substitute them into the integral matrix representation in Eq. (1) to get [35]:

$$\mathbb{W}_\alpha(\mathbf{r}, \mathbf{p}) = \mathbb{M} W_\alpha(\mathbf{r}, \mathbf{p}) \mathbb{M}^\dagger. \tag{36}$$

Thus, the trace of this matrix provides us an expression of the time-dependent WF of the coherent states:

$$\mathrm{Tr}[\mathbb{W}_\alpha(\mathbf{r}, \mathbf{p}, t)] = \mathcal{N}_\alpha^2\, \delta(p_y - k_y) \Big\{ W_{11}(\chi, t) + W_{22}(\chi, t) - 2\lambda\beta_\nu \Re[W_{12}(\chi, t)] \Big\}, \tag{37}$$

where the components W_{11}, W_{22} and W_{12} are the corresponding Wigner functions of the terms in Eq. (34) and their product, and that in general involve sums

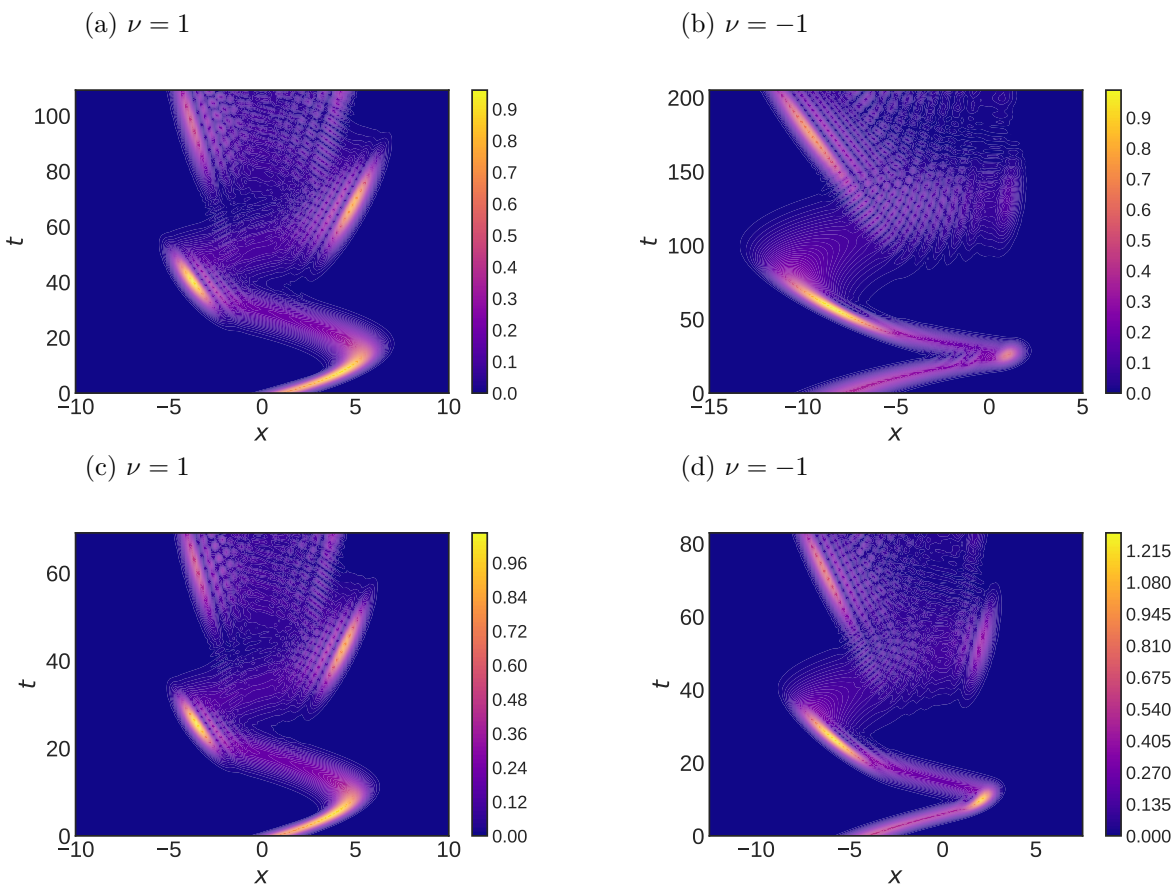

FIGURE 3. Time evolution of the probability density $|\Psi_\alpha(\mathbf{r},t)|^2$ in Eq. (35) with $k_y = 0$, $B = 1$, $\alpha = 4i$, $\mathcal{E} = 0.25$ and $\lambda = 1$ for 8B $-pmmn$ borophene (a, b) and 2BH $-pmmn$ borophene (c, d) in each Dirac point ($\nu = \pm 1$).

of functions of the form (see [35] for more details)

$$W_{u,v}(\chi_{n,m}) = \frac{1}{\pi}\exp\left(-\frac{1}{2}|\chi_{n,m}|^2 + i(\zeta_n - \zeta_m)s\right) \times \begin{cases} (-1)^u\sqrt{\frac{u!}{v!}}\chi_{n,m}^{v-u}L_u^{v-u}\left(|\chi_{n,m}|^2\right), & \text{if } u \le v, \\ (-1)^v\sqrt{\frac{v!}{u!}}\chi_{n,m}^{*u-v}L_v^{u-v}\left(|\chi_{n,m}|^2\right), & \text{if } u \ge v, \end{cases} \tag{38}$$

with $L_n^m(\cdot)$ denoting the associated Laguerre polynomials, and

$$\chi_{n,m} = \frac{\zeta_n + \zeta_m}{\sqrt{2}} + i\sqrt{2}\,s, \quad \chi_n \equiv \chi_{n,n}, \tag{39a}$$

$$s = \left(1 - \beta_\nu^2\right)^{-1/4}\sqrt{\frac{2v_x}{\omega_B v_y}}\,p_x. \tag{39b}$$

The time evolution of the WM trace for the CSs is shown in Figures 4 and 5 for 8B and 2BH $-pmmn$ borophene, respectively. In both cases, we observe that the WF in valley K propagates faster than in valley K'. As the state evolves in time, the trace of the WM takes negative values, which is an indication of the increasing of the CS quantumness and also of the uncertainty relations, as is discussed in [35]. For larger times, the WM traces become identical to that of the Landau state with n equal to the integer part of $|\alpha|^2$, in agreement to the number occupation distribution in Eq. (30).

3.5.1. PERIOD OF MOTION

Now, in order to provide an approximate period τ for the CSs, we proceed as follows [85]. First, we calculate the mean energy $\langle H\rangle_\alpha$ for the CSs $\bar{\Psi}_\alpha(\mathbf{r})$. Then, setting the eigenvalue z, we compute the energy interval in which $\langle H\rangle_\alpha$ lies, namely, $E_{j,k_y} < \langle H\rangle_\alpha < E_{j+1,k_y}$. Thus, the approximate period is determined as:

$$\tau = \frac{2\pi}{\Delta E} = \frac{2\pi}{E_{j+1,k_y} - E_{j,k_y}}, \tag{40}$$

that will be different for each valley since the energy spectrum depends on the tilting parameter ν. For instance, for the CSs with $\alpha = 4i$ and the same values used in Figures 3, 4 and 5, we have $E_{15} < \langle H\rangle_\alpha < E_{16}$. Note that $\langle H\rangle_\alpha$ is bounded by the Landau level with $n = |\alpha|^2 = 16$. Thus, the respective periods are reported in Table 3.

The period τ in Eq. (40) increases as $\Delta E \to 0$ close to the electric field critical value $\mathcal{E}_c$, since a Dirac fermion takes a longer time to complete a loop an opened orbit (see red and blue curves in Figure 6). In contrast, the orbits are closed for more separated energy levels resulting in a shorter period τ (see green curve in Figure 6).

(a) $t = 0$, $\nu = 1$ (b) $t = 0$, $\nu = -1$

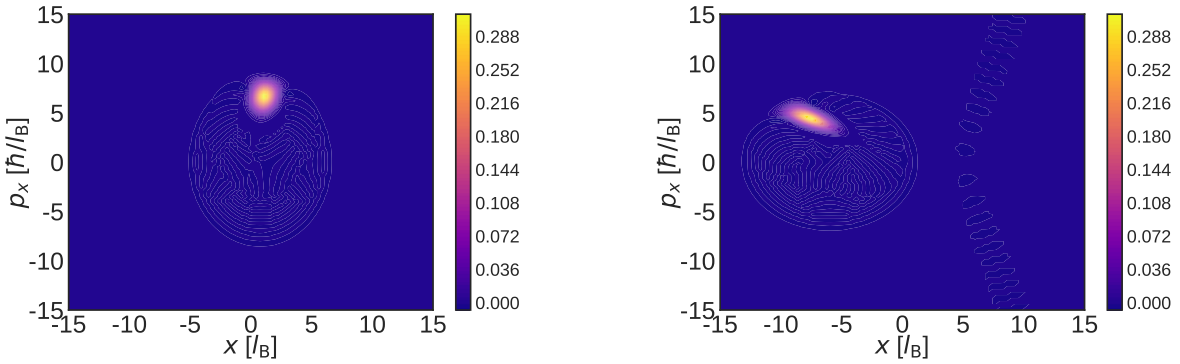

(c) $t = 15$, $\nu = 1$ (d) $t = 15$, $\nu = -1$

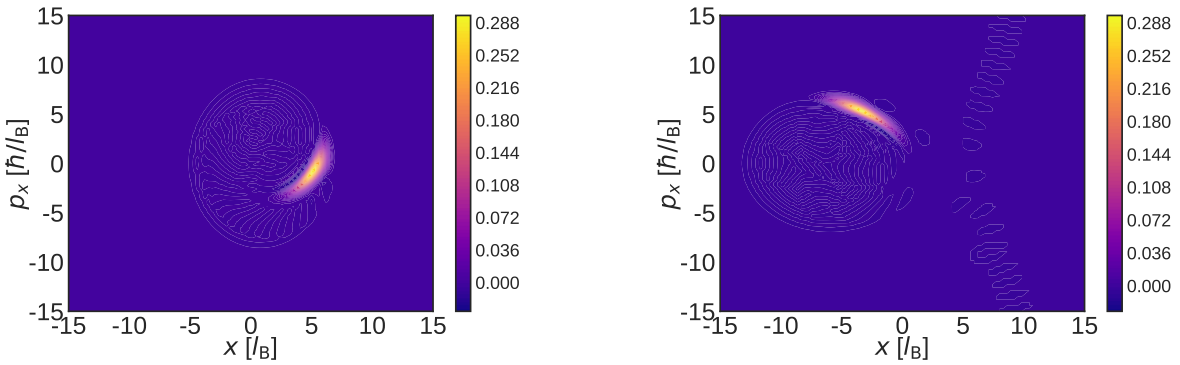

(e) $t = 30$, $\nu = 1$ (f) $t = 30$, $\nu = -1$

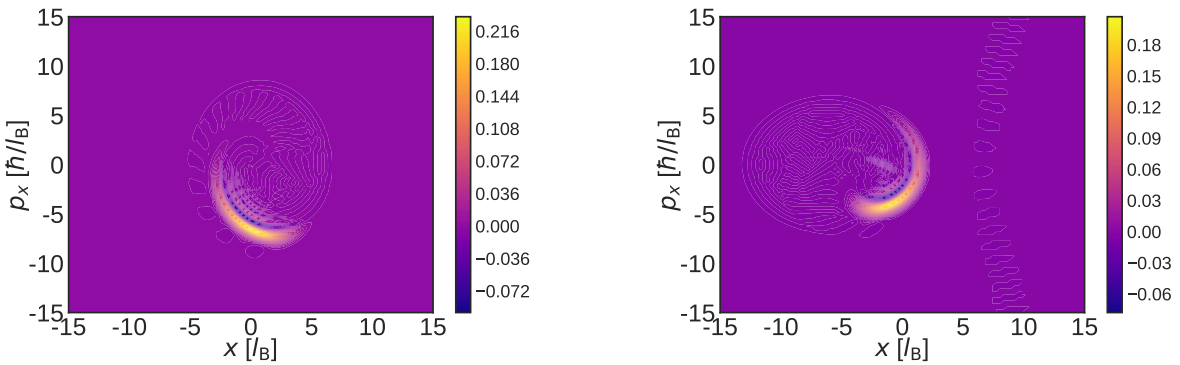

(g) $t = 45$, $\nu = 1$ (h) $t = 45$, $\nu = -1$

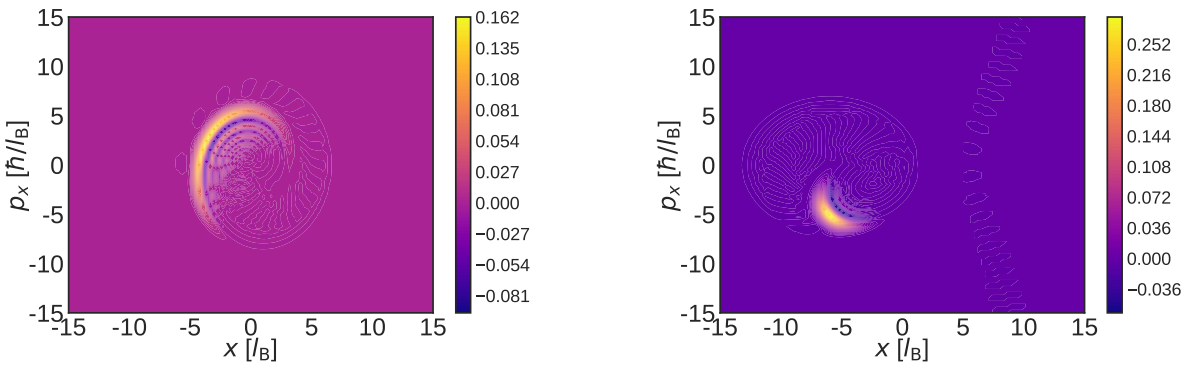

FIGURE 4. Time evolution of the trace of the Wigner matrix $\mathbb{W}_\alpha(\mathbf{r}, \mathbf{p})$ in Eq. (37) for different values of t in each Dirac point ($\nu = \pm 1$) of 8B $-pmmn$ borophene. $B = 1$, $k_y = 0$, $\alpha = 4i$, $\{v_x, v_y, v_t\} = \{0.534, 0.785, -0.345\}$, $\mathcal{E} = 0.25$, and $\lambda = 1$. In the figure labels, $l_B = 1/\sqrt{B}$.

(a) $t = 0$, $\nu = 1$

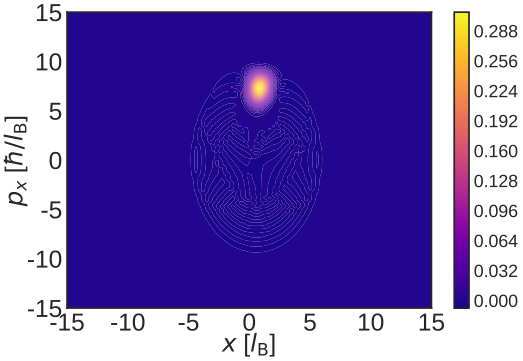

(b) $t = 0$, $\nu = -1$

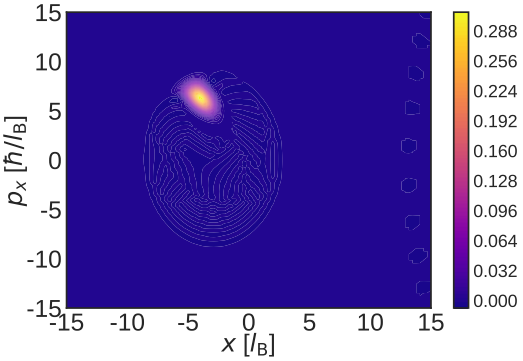

(c) $t = 15$, $\nu = 1$

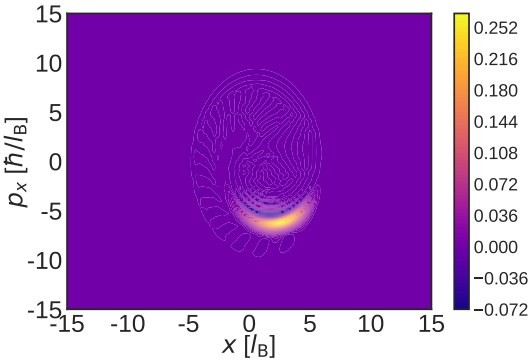

(d) $t = 15$, $\nu = -1$

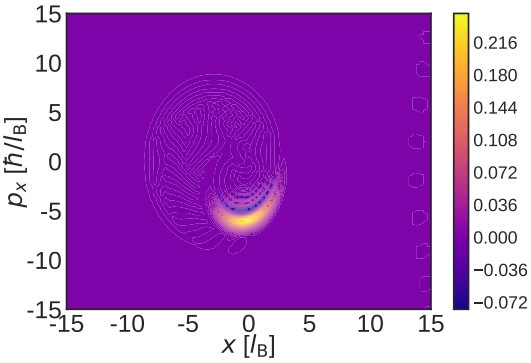

(e) $t = 30$, $\nu = 1$

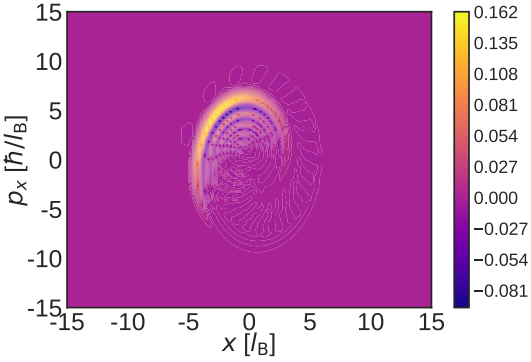

(f) $t = 30$, $\nu = -1$

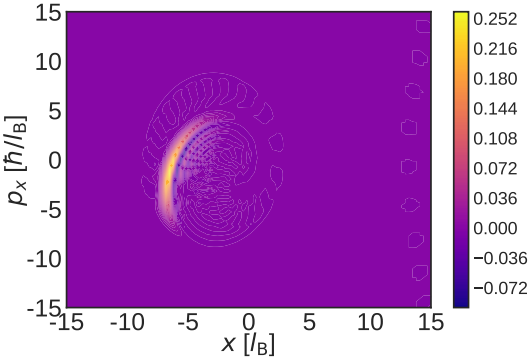

(g) $t = 45$, $\nu = 1$

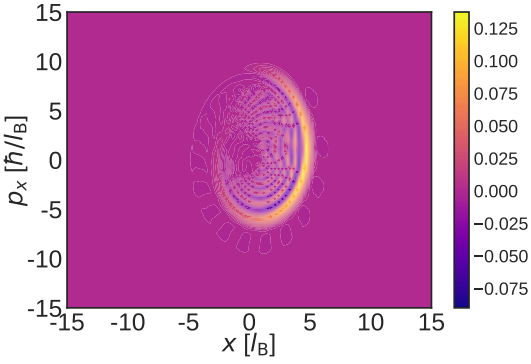

(h) $t = 45$, $\nu = -1$

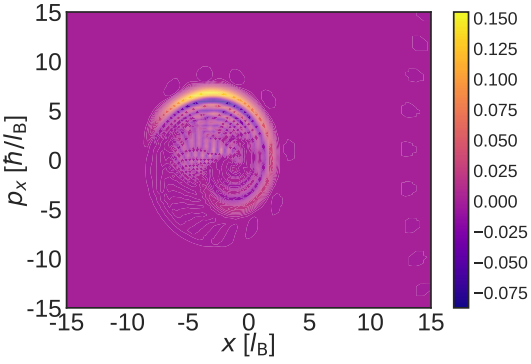

FIGURE 5. Time evolution of the trace of the Wigner matrix $\mathbb{W}_\alpha(\mathbf{r}, \mathbf{p})$ in Eq. (37) for different values of t in each Dirac point ($\nu = \pm 1$) of 2BH $-pmmn$ borophene. $B = 1$, $k_y = 0$, $\alpha = 4i$, $\{v_x, v_y, v_t\} = \{0.77, 1.348, -0.380\}$, $\mathcal{E} = 0.25$, and $\lambda = 1$. In the figure labels, $l_B = 1/\sqrt{B}$.

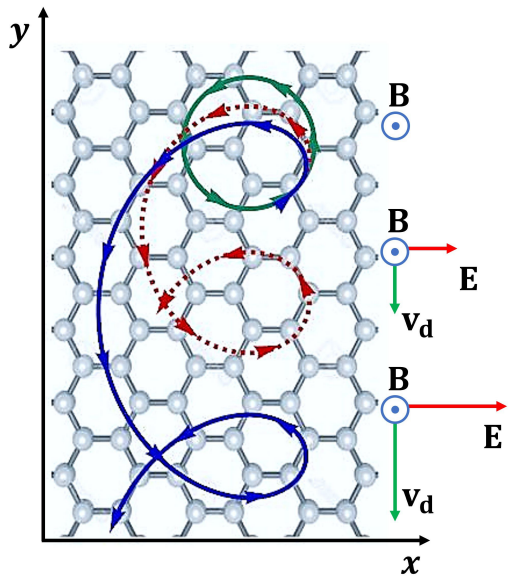

Figure 6. A generic honeycomb lattice interacts with crossed electric and magnetic fields directed along the x- and z-directions, respectively. In absence of electric field $\mathbf{E}$, a non-relativistic classical charged particle performs a circular trajectory (green curve), while if the strength $\mathbf{E}$ increases, the trajectory becomes into a trochoid (red and blue curves). The drift velocity $\mathbf{v}_\mathrm{d} = \mathbf{E} \times \mathbf{B}/B^2$ is directed along the y-direction.

Borophene monolayer	τ_+ (K)	τ_- (K')
$8-pmmn$	34.165π	14.566π
$8\mathrm{B}-pmmn$	17.388π	32.642π
$2\mathrm{BH}-pmmn$	11.012π	13.200π

Table 3. Valley-dependent period τ for the CSs with eigenvalue $\alpha = 4i = z/\sqrt{2}$ in three boron allotropes. The data for $8-pmmn$ borophene were obtained from [35].

3.6. Discussion

Anisotropic and tilted Dirac cone materials, such as 8B and $2\mathrm{BH}-pmmn$ borophene, possess valley-dependent electronic properties under the interaction with crossed electric and magnetic fields. The effective Hamiltonian depends on two anisotropic velocities and one tilt velocity (see Eq. (2)). In the case in which these materials interact with external crossed electric and magnetic fields (see Eq. (4)), it is possible to obtain the solutions to the physical problem in a simple algebraic way (see Eq. (15) and (17)).

We have constructed the CSs $\bar{\Psi}_\alpha(\mathbf{r})$ as a linear combination of the Landau eigenfunctions $\bar{\Psi}(\mathbf{r})$ of the Hamiltonian in Eq. (4), that also be eigenfunction of a matrix ladder operator $\mathbb{B}^-$ with a complex eigenvalue z. As the coherent electron states evolve in time, their probability density clearly shows maximum values only around the turning points in the x-axis, in which momentarily the velocity of charge carriers reduces. In turn, the emergence of negative values in the trace of the Wigner matrix for longer times is related to the increasing uncertainties of the position and momentum, as is studied in [35], in agreement to the probability distribution Eq. (30). Also, the increasing of the electric field to a critical value can delay the time-evolution of CSs in one of the valleys, allowing us to distinguish the Dirac fermions of one valley from those of another (see Figures 3, 4 and 5).

In Figure 6, we have showed the classical picture of a (valley-independent) non-relativistic charge carrier that follows a closed trajectory in the xy-plane in presence of an external magnetic field $\mathbf{B}$ along the z-direction. When an electric field $\mathbf{E}$ is applied along the x-axis, the trajectory becomes into a trochoid with velocity $\mathbf{v}_\mathrm{d}$ directed to the y-direction. In contrast, we observe that in the quantum picture of our problem, due to the Lorentz transformation into the reference frame and the energy [43], as well as the valley index, there is a factor $(1-\beta_\nu^2)^{3/4}$ that modifies the spacing between two adjacent Landau levels, and as a consequence also the period of motion in Eq. (40).

4. Conclusions

We studied the dynamics of massless Dirac fermions in two bidimensional monolayers of boron allotropes under the interaction with crossed external electric and magnetic fields. We analyzed the effect of the Dirac cone tilt in the time evolution of probability density of coherent electron states as well as the corresponding Wigner function. We conclude that the time evolution of the coherent electron states in these materials is valley dependent, and the presence of an in-plane external electric field reinforces such a dependency.

We consider that the findings here presented may contribute to the understanding of the effects of the tilting of the Dirac cones 8B and $2\mathrm{BH}-pmmn$ borophene on the charge carrier dynamics under the interaction of electromagnetic fields, with which these materials could be considered as viable valley splitters in experimental applications. Besides, the coherent state description developed through the phase-space representation may provide a satisfactory semi-classical description of similar quantum valley-dependent phenomena that occur in other tilted anisotropic Dirac materials interacting with external electromagnetic fields.

Acknowledgements

The author acknowledges T. Stegmann and Y. Betancur-Ocampo for their invaluable comments to improve this work, as well as the financial support from CONACYT Project FORDECYT-PRONACES/61533/2020 and SIP-IPN research grant 20210317.

References

[1] E. Schrödinger. Der stetige Übergang von der Mikro- zur Makromechanik. *Naturwissenschaften* **14**(28):664–666, 1926. https://doi.org/10.1007/BF01507634.

[2] R. J. Glauber. Coherent and incoherent states of the radiation field. *Physical Review* **131**:2766–2788, 1963. https://doi.org/10.1103/PhysRev.131.2766.

[3] J. Weinbub, D. K. Ferry. Recent advances in Wigner function approaches. *Applied Physics Reviews* **5**(4):041104, 2018. https://doi.org/10.1063/1.5046663.

[4] C. Gerry, P. Knight, C. C. Gerry. *Introductory Quantum Optics*. Cambridge University Press, 2010. ISBN 052152735X.

[5] E. Wigner. On the quantum correction for thermodynamic equilibrium. *Physical Review* **40**(5):749–759, 1932. https://doi.org/10.1103/physrev.40.749.

[6] M. Hillery, R. F. O'Connell, M. O. Scully, E. P. Wigner. Distribution functions in physics: Fundamentals. *Physics Reports* **106**(3):121–167, 1984. https://doi.org/10.1016/0370-1573(84)90160-1.

[7] A. Kenfack, K. Zyczkowski. Negativity of the Wigner function as an indicator of non-classicality. *Journal of Optics B: Quantum and Semiclassical Optics* **6**(10):396–404, 2004. https://doi.org/10.1088/1464-4266/6/10/003.

[8] D. T. Smithey, M. Beck, M. G. Raymer, A. Faridani. Measurement of the Wigner distribution and the density matrix of a light mode using optical homodyne tomography: Application to squeezed states and the vacuum. *Physical Review Letters* **70**(9):1244–1247, 1993. https://doi.org/10.1103/physrevlett.70.1244.

[9] C. Baune, J. Fiurášek, R. Schnabel. Negative Wigner function at telecommunication wavelength from homodyne detection. *Physical Review A* **95**(6):061802, 2017. https://doi.org/10.1103/physreva.95.061802.

[10] H.-W. Lee. Theory and application of the quantum phase-space distribution functions. *Physics Reports* **259**(3):147–211, 1995. https://doi.org/10.1016/0370-1573(95)00007-4.

[11] W. B. Case. Wigner functions and Weyl transforms for pedestrians. *American Journal of Physics* **76**(10):937–946, 2008. https://doi.org/10.1119/1.2957889.

[12] R. P. Rundle, P. W. Mills, T. Tilma, et al. Simple procedure for phase-space measurement and entanglement validation. *Physical Review A* **96**(2):022117, 2017. https://doi.org/10.1103/physreva.96.022117.

[13] M. V. Berry. Semi-classical mechanics in phase space: A study of Wigner's function. *Philosophical Transactions of the Royal Society of London Series A, Mathematical and Physical Sciences* **287**(1343):237–271, 1977. https://doi.org/10.1098/rsta.1977.0145.

[14] C. Jacoboni, P. Bordone. The Wigner-function approach to non-equilibrium electron transport. *Reports on Progress in Physics* **67**(7):1033, 2004. https://doi.org/10.1088/0034-4885/67/7/r01.

[15] C. Bäuerle, D. C. Glattli, T. Meunier, et al. Coherent control of single electrons: a review of current progress. *Reports on Progress in Physics* **81**(5):056503, 2018. https://doi.org/10.1088/1361-6633/aaa98a.

[16] E. Colomés, Z. Zhan, X. Oriols. Comparing Wigner, Husimi and Bohmian distributions: which one is a true probability distribution in phase space? *Journal of Computational Electronics* **14**(4):894–906, 2015. https://doi.org/10.1007/s10825-015-0737-6.

[17] D. J. Mason, M. F. Borunda, E. J. Heller. Revealing the flux: Using processed Husimi maps to visualize dynamics of bound systems and mesoscopic transport. *Physical Review B* **91**(16):165405, 2015. https://doi.org/10.1103/physrevb.91.165405.

[18] C. M. Carmesin, P. Kling, E. Giese, et al. Quantum and classical phase-space dynamics of a free-electron laser. *Physical Review Research* **2**(2):023027, 2020. https://doi.org/10.1103/physrevresearch.2.023027.

[19] O. Morandi, F. Schürrer. Wigner model for quantum transport in graphene. *Journal of Physics A: Mathematical and Theoretical* **44**(26):265301, 2011. https://doi.org/10.1088/1751-8113/44/26/265301.

[20] E. Díaz-Bautista, Y. Betancur-Ocampo. Phase-space representation of Landau and electron coherent states for uniaxially strained graphene. *Physical Review B* **101**(12):125402, 2020. https://doi.org/10.1103/physrevb.101.125402.

[21] E. Díaz-Bautista, Y. Concha-Sánchez, A. Raya. Barut–Girardello coherent states for anisotropic 2D-Dirac materials. *Journal of Physics: Condensed Matter* **31**(43):435702, 2019. https://doi.org/10.1088/1361-648x/ab2d18.

[22] E. Díaz-Bautista, D. J. Fernández. Graphene coherent states. *The European Physical Journal Plus* **132**(11):499, 2017. https://doi.org/10.1140/epjp/i2017-11794-y.

[23] D. J. Mason, M. F. Borunda, E. J. Heller. Semiclassical deconstruction of quantum states in graphene. *Physical Review B* **88**(16):165421, 2013. https://doi.org/10.1103/physrevb.88.165421.

[24] G. J. Iafrate, V. N. Sokolov, J. B. Krieger. Quantum transport and the Wigner distribution function for Bloch electrons in spatially homogeneous electric and magnetic fields. *Physical Review B* **96**(14):144303, 2017. https://doi.org/10.1103/physrevb.96.144303.

[25] P. Ghosh, P. Roy. Quasi coherent state of the Dirac oscillator. *Journal of Modern Optics* **68**(1):56–62, 2021. https://doi.org/10.1080/09500340.2021.1876261.

[26] D. K. Ferry, I. Welland. Relativistic Wigner functions in transition metal dichalcogenides. *Journal of Computational Electronics* **17**(1):110–117, 2017. https://doi.org/10.1007/s10825-017-1094-4.

[27] E. Díaz-Bautista, M. Oliva-Leyva. Coherent states for dispersive pseudo-Landau-levels in strained honeycomb lattices. *The European Physical Journal Plus* **136**(7):765, 2021. https://doi.org/10.1140/epjp/s13360-021-01753-w.

[28] J. R. Schaibley, H. Yu, G. Clark, et al. Valleytronics in 2D materials. *Nature Reviews Materials* **1**(11):16055, 2016. https://doi.org/10.1038/natrevmats.2016.55.

[29] A. Kundu, H. A. Fertig, B. Seradjeh. Floquet-engineered valleytronics in Dirac systems. *Physical Review Letters* **116**:016802, 2016. https://doi.org/10.1103/PhysRevLett.116.016802.

[30] Y. S. Ang, S. A. Yang, C. Zhang, et al. Valleytronics in merging Dirac cones: All-electric-controlled valley filter, valve, and universal reversible logic gate. *Physical Review B* **96**:245410, 2017. https://doi.org/10.1103/PhysRevB.96.245410.

[31] A. Lopez-Bezanilla, P. B. Littlewood. Electronic properties of 8−*Pmmn* borophene. *Physical Review B* **93**(24):241405, 2016. https://doi.org/10.1103/physrevb.93.241405.

[32] A. D. Zabolotskiy, Y. E. Lozovik. Strain-induced pseudomagnetic field in the Dirac semimetal borophene. *Physical Review B* **94**(16):165403, 2016. https://doi.org/10.1103/physrevb.94.165403.

[33] SK Firoz Islam, A. M. Jayannavar. Signature of tilted Dirac cones in weiss oscillations of 8 − *Pmmn* borophene. *Physical Review B* **96**(23):235405, 2017. https://doi.org/10.1103/physrevb.96.235405.

[34] SK Firoz Islam. Magnetotransport properties of 8-Pmmn borophene: effects of Hall field and strain. *Journal of Physics: Condensed Matter* **30**(27):275301, 2018. https://doi.org/10.1088/1361-648x/aac8b3.

[35] Y. Betancur-Ocampo, E. Díaz-Bautista, T. Stegmann. Valley-dependent time evolution of coherent electron states in tilted anisotropic Dirac materials. *Physical Review B* **105**(4):045401, 2022. https://doi.org/10.1103/PhysRevB.105.045401.

[36] M. Assili, S. Haddad, W. Kang. Electric field-induced valley degeneracy lifting in uniaxial strained graphene: Evidence from magnetophonon resonance. *Physical Review B* **91**(11):115422, 2015. https://doi.org/10.1103/physrevb.91.115422.

[37] D. Sabsovich, T. Meng, D. I. Pikulin, et al. Pseudo field effects in type II Weyl semimetals: new probes for over tilted cones. *Journal of Physics: Condensed Matter* **32**(48):484002, 2020. https://doi.org/10.1088/1361-648x/abaa7e.

[38] K. Das, A. Agarwal. Linear magnetochiral transport in tilted type-I and type-II Weyl semimetals. *Physical Review B* **99**(8):085405, 2019. https://doi.org/10.1103/physrevb.99.085405.

[39] A. Menon, B. Basu. Anomalous Hall transport in tilted multi-Weyl semimetals. *Journal of Physics: Condensed Matter* **33**(4):045602, 2020. https://doi.org/10.1088/1361-648x/abb9b8.

[40] P. P. Ferreira, A. L. R. Manesco, T. T. Dorini, et al. Strain engineering the topological type-II Dirac semimetal $NiTe_2$. *Physical Review B* **103**(12):125134, 2021. https://doi.org/10.1103/physrevb.103.125134.

[41] J. Sári, M. O. Goerbig, C. Tőke. Magneto-optics of quasirelativistic electrons in graphene with an inplane electric field and in tilted Dirac cones in α-(BEDT TTF)$_2$I$_3$. *Physical Review B* **92**(3):035306, 2015. https://doi.org/10.1103/physrevb.92.035306.

[42] M. O. Goerbig, J.-N. Fuchs, G. Montambaux, F. Piéchon. Tilted anisotropic Dirac cones in quinoid-type graphene and α-(BEDT-TTF)$_2$I$_3$. *Physical Review B* **78**(4):045415, 2008. https://doi.org/10.1103/physrevb.78.045415.

[43] M. O. Goerbig, J.-N. Fuchs, G. Montambaux, F. Piéchon. Electric-field–induced lifting of the valley degeneracy in α-(BEDT-TTF)$_2$I$_3$ Dirac-like Landau levels. *EPL Europhysics Letters* **85**(5):57005, 2009. https://doi.org/10.1209/0295-5075/85/57005.

[44] T. Morinari, T. Himura, T. Tohyama. Possible verification of tilted anisotropic Dirac cone in α-(BEDT-TTF)$_2$I$_3$ using interlayer magnetoresistance. *Journal of the Physical Society of Japan* **78**(2):023704, 2009. https://doi.org/10.1143/jpsj.78.023704.

[45] X.-F. Zhou, X. Dong, A. R. Oganov, et al. Semimetallic two-dimensional boron allotrope with massless Dirac fermions. *Physical Review Letters* **112**(8):085502, 2014. https://doi.org/10.1103/physrevlett.112.085502.

[46] A. J. Mannix, X.-F. Zhou, B. Kiraly, et al. Synthesis of borophenes: Anisotropic, two-dimensional boron polymorphs. *Science* **350**(6267):1513–1516, 2015. https://doi.org/10.1126/science.aad1080.

[47] B. Feng, J. Zhang, Q. Zhong, et al. Experimental realization of two-dimensional boron sheets. *Nature Chemistry* **8**(6):563–568, 2016. https://doi.org/10.1038/nchem.2491.

[48] W. Li, L. Kong, C. Chen, et al. Experimental realization of honeycomb borophene. *Science Bulletin* **63**(5):282–286, 2018. https://doi.org/10.1016/j.scib.2018.02.006.

[49] Z.-Q. Wang, T.-Y. Lü, H.-Q. Wang, et al. Review of borophene and its potential applications. *Frontiers of Physics* **14**(3):33403, 2019. https://doi.org/10.1007/s11467-019-0884-5.

[50] S.-H. Zhang, W. Yang. Oblique Klein tunneling in 8-*Pmmn* borophene $p-n$ junctions. *Physical Review B* **97**(23):235440, 2018. https://doi.org/10.1103/physrevb.97.235440.

[51] S.-H. Zhang, W. Yang. Anomalous caustics and Veselago focusing in 8-*pmmn* borophene p–n junctions with arbitrary junction directions. *New Journal of Physics* **21**(10):103052, 2019. https://doi.org/10.1088/1367-2630/ab4d8f.

[52] N. Tajima, K. Kajita. Experimental study of organic zero-gap conductor α-(BEDT-TTF)$_2$I$_3$. *Science and Technology of Advanced Materials* **10**(2):024308, 2009. https://doi.org/10.1088/1468-6996/10/2/024308.

[53] N. P. Armitage, E. J. Mele, A. Vishwanath. Weyl and Dirac semimetals in three-dimensional solids. *Reviews of Modern Physics* **90**(1):015001, 2018. https://doi.org/10.1103/revmodphys.90.015001.

[54] Y. Betancur-Ocampo, F. Leyvraz, T. Stegmann. Electron optics in phosphorene pn junctions: Negative reflection and anti-super-Klein tunneling. *Nano Lett* **19**(11):7760–7769, 2019. https://doi.org/10.1021/acs.nanolett.9b02720.

[55] Y. Betancur-Ocampo, E. Paredes-Rocha, T. Stegmann. Phosphorene pnp junctions as perfect electron waveguides. *Journal of Applied Physics* **128**(11):114303, 2020. https://doi.org/10.1063/5.0019215.

[56] N. Levy, S. A. Burke, K. L. Meaker, et al. Strain-induced pseudo-magnetic fields greater than 300 tesla in graphene nanobubbles. *Science* **329**(5991):544–547, 2010. https://doi.org/10.1126/science.1191700.

[57] F. Guinea, M. I. Katsnelson, A. K. Geim. Energy gaps and a zero-field quantum Hall effect in graphene by strain engineering. *Nature Physics* **6**(1):30–33, 2009. https://doi.org/10.1038/nphys1420.

[58] S. H. R. Sena, J. M. Pereira Jr, G. A. Farias, et al. The electronic properties of graphene and graphene ribbons under simple shear strain. *Journal of Physics: Condensed Matter* **24**(37):375301, 2012. https://doi.org/10.1088/0953-8984/24/37/375301.

[59] P. Ghosh, P. Roy. Collapse of Landau levels in graphene under uniaxial strain. *Materials Research Express* **6**(12):125603, 2019. https://doi.org/10.1088/2053-1591/ab52ad.

[60] V. M. Pereira, A. H. Castro Neto. Strain engineering of graphene's electronic structure. *Physical Review Letters* **103**(4):046801, 2009. https://doi.org/10.1103/physrevlett.103.046801.

[61] V. M. Pereira, A. H. Castro Neto, N. M. R. Peres. Tight-binding approach to uniaxial strain in graphene. *Physical Review B* **80**(4):045401, 2009. https://doi.org/10.1103/physrevb.80.045401.

[62] G. Cocco, E. Cadelano, L. Colombo. Gap opening in graphene by shear strain. *Physical Review B* **81**(24):241412, 2010. https://doi.org/10.1103/physrevb.81.241412.

[63] F. M. D. Pellegrino, G. G. N. Angilella, R. Pucci. Strain effect on the optical conductivity of graphene. *Physical Review B* **81**(3):035411, 2010. https://doi.org/10.1103/physrevb.81.035411.

[64] H. Rostami, R. Asgari. Electronic ground-state properties of strained graphene. *Physical Review B* **86**(15):155435, 2012. https://doi.org/10.1103/physrevb.86.155435.

[65] S. Barraza-Lopez, A. A. Pacheco Sanjuan, Z. Wang, M. Vanević. Strain-engineering of graphene's electronic structure beyond continuum elasticity. *Solid State Communications* **166**:70–75, 2013. https://doi.org/10.1016/j.ssc.2013.05.002.

[66] G. G. Naumis, S. Barraza-Lopez, M. Oliva-Leyva, H. Terrones. Electronic and optical properties of strained graphene and other strained 2D materials: a review. *Reports on Progress in Physics* **80**(9):096501, 2017. https://doi.org/10.1088/1361-6633/aa74ef.

[67] D.-N. Le, V.-H. Le, P. Roy. Graphene under uniaxial inhomogeneous strain and an external electric field: Landau levels, electronic, magnetic and optical properties. *The European Physical Journal B* **93**(8):158, 2020. https://doi.org/10.1140/epjb/e2020-10222-3.

[68] S. M. Cunha, D. R. da Costa, L. C. Felix, et al. Electronic and transport properties of anisotropic semiconductor quantum wires. *Physical Review B* **102**(4):045427, 2020. https://doi.org/10.1103/physrevb.102.045427.

[69] T. Stegmann, N. Szpak. Current flow paths in deformed graphene: from quantum transport to classical trajectories in curved space. *New Journal of Physics* **18**(5):053016, 2016. https://doi.org/10.1088/1367-2630/18/5/053016.

[70] T. Stegmann, N. Szpak. Current splitting and valley polarization in elastically deformed graphene. *2D Materials* **6**(1):015024, 2019. https://doi.org/10.1088/2053-1583/aaea8d.

[71] Y. Betancur-Ocampo. Partial positive refraction in asymmetric Veselago lenses of uniaxially strained graphene. *Physical Review B* **98**(20):205421, 2018. https://doi.org/10.1103/physrevb.98.205421.

[72] Y. Betancur-Ocampo, P. Majari, D. Espitia, et al. Anomalous floquet tunneling in uniaxially strained graphene. *Physical Review B* **103**(15):155433, 2021. https://doi.org/10.1103/physrevb.103.155433.

[73] T. Cheng, H. Lang, Z. Li, et al. Anisotropic carrier mobility in two-dimensional materials with tilted Dirac cones: theory and application. *Physical Chemistry Chemical Physics* **19**:23942–23950, 2017. https://doi.org/10.1039/C7CP03736H.

[74] B. Feng, J. Zhang, R.-Y. Liu, et al. Direct evidence of metallic bands in a monolayer boron sheet. *Physical Review B* **94**:041408, 2016. https://doi.org/10.1103/PhysRevB.94.041408.

[75] Y. Zhao, X. Li, J. Liu, et al. A new anisotropic Dirac cone material: A B_2S honeycomb monolayer. *The Journal of Physical Chemistry Letters* **9**(7):1815–1820, 2018. https://doi.org/10.1021/acs.jpclett.8b00616.

[76] D. Ferraro, B. Roussel, C. Cabart, et al. Real-time decoherence of Landau and Levitov quasiparticles in quantum hall edge channels. *Physical Review Letters* **113**(16):166403, 2014. https://doi.org/10.1103/physrevlett.113.166403.

[77] T. Jullien, P. Roulleau, B. Roche, et al. Quantum tomography of an electron. *Nature* **514**(7524):603–607, 2014. https://doi.org/10.1038/nature13821.

[78] J. Oertel. *Solutions of the Dirac equation in spacetime-dependent electric fields.* Master's thesis, University of Duisburg-Essen, Freiberg, Germany, 2014.

[79] M. Castillo-Celeita, E. Díaz-Bautista, M. Oliva-Leyva. Coherent states for graphene under the interaction of crossed electric and magnetic fields. *Annals of Physics* **421**:168287, 2020. https://doi.org/10.1016/j.aop.2020.168287.

[80] V. Lukose, R. Shankar, G. Baskaran. Novel electric field effects on Landau levels in graphene. *Physical Review Letters* **98**(11):116802, 2007. https://doi.org/10.1103/physrevlett.98.116802.

[81] N. Gu, M. Rudner, A. Young, et al. Collapse of Landau levels in gated graphene structures. *Physical Review Letters* **106**(6):066601, 2011. https://doi.org/10.1103/physrevlett.106.066601.

[82] J. M. Ziman. *Principles of the Theory of Solids.* Cambridge University Press, 2nd edn., 1972. https://doi.org/10.1017/CBO9781139644075.

[83] T. Huang, R. Chen, T. Ma, et al. Electronic Bloch oscillation in a pristine monolayer graphene. *Physics Letters A* **382**(42-43):3086–3089, 2018. https://doi.org/10.1016/j.physleta.2018.07.035.

[84] M. Kai, W. Jian-Hua, Y. Yi. Wigner function for the Dirac oscillator in spinor space. *Chinese Physics C* **35**(1):11–15, 2011. https://doi.org/10.1088/1674-1137/35/1/003.

[85] D. J. Fernández, D. I. Martínez-Moreno. Bilayer graphene coherent states. *The European Physical Journal Plus volume* **135**(9):739, 2020. https://doi.org/10.1140/epjp/s13360-020-00746-5.